Eddy Convection in Coaxial Supersonic Jets

Erina Murakami[*] and Dimitri Papamoschou[†]
University of California, Irvine, Irvine, California 92697-3975

We present experimental results on the morphology and evolution of large turbulent eddies in coaxial supersonic jets. The study encompassed Mach 1.5, axisymmetric, perfectly expanded jets composed of air or a mixture of helium and air. A double-exposure planar laser-induced fluorescence (PLIF) system, with gaseous acetone as the tracer molecule, enabled visualization of the turbulent structure and of its evolution a short time later. The convective velocity of the eddies was extracted from the PLIF images by means of two-dimensional cross correlations. Eddies in the air jet propagate with a speed approximately 80% of the local centerline mean velocity. In the faster helium-air jets eddies are measured to be supersonic with respect to the ambient air, a result corroborated by the visualization of Mach waves. In the helium-air jet addition of a Mach 0.82 secondary flow reduces the convective velocity of the primary eddies from 70 to 62% of the primary exit velocity. The speed of the secondary eddies is 44% of the secondary exit velocity. All turbulent motions in this coaxial helium-air jet are intrinsically subsonic, leading to substantial reduction of Mach waves and reduction in noise. A refined empirical model for eddy convection in compressible jets is proposed. The results of this study are relevant to mixing, combustion, and jet noise.

I. Introduction

LARGE-SCALE motions are present in every turbulent flow of practical significance. These motions, or eddies, play a substantial role in mixing, combustion, and noise production. The organized, coherent nature of large eddies in subsonic shear layers was vividly captured in the visualizations of Brown and Roshko[1] and has since been the subject of numerous theoretical and experimental works. Strong parallels between the development of vortex-sheet (Kelvin–Helmholtz) instability and the behavior of fully turbulent shear layers suggest that large eddies constitute the dominant instability of the flow.[2,3] A key aspect of the instability is its phase speed or convective velocity U_c. In subsonic shear layers U_c controls the entrainment ratio and influences the growth rate.[4] In high-speed shear layers and jets the value of U_c governs the generation of strong sources of sound.

In compressible mixing layers, large eddies lose their organization but are still ubiquitous.[5] The compressibility of mixing layers is characterized by the Mach number in the frame of reference of the instability, called the convective Mach number. For an instability wave traveling with a velocity U_c between a fast stream (1) and a slow stream (2), the convective Mach number takes the values

$$M_{c_1} = (U_1 - U_c)/a_1, \qquad M_{c_2} = (U_c - U_2)/a_2 \qquad (1)$$

with respect to the fast and slow streams, respectively, where U is the freestream velocity and a is the freestream speed of sound.[6] A symmetric Lagrangian model for the large structure,[6] where the two freestreams suffer zero or equal total-pressure loss as they are entrained toward a common stagnation point inside the mixing region, gives

$$M_{c_1} = M_{c_2} = (U_1 - U_2)/(a_1 + a_2) \qquad (2)$$

Equation (2) is exact for streams having equal specific heat ratios ($\gamma_1 = \gamma_2$) and requires a slight correction, too small to be of practical significance here, for $\gamma_1 \neq \gamma_2$. The corresponding convective velocity is

$$U_{c_\mathrm{sym}} = U_1\left[(1 + r\sqrt{s})^| (1 + \sqrt{s})\right] \qquad (3)$$

where $r = U_2/U_1$ and $s = \rho_2/\rho_1$. Recent experiments in which the convective velocity was measured[7–9] have shown that the predictions of Eqs. (2) and (3) are inaccurate at high compressibility. Instead of the symmetry expected from Eq. (2), eddies behave asymmetrically, with fast modes (high M_{c_2}, low M_{c_1}) in shear layers between a supersonic and a subsonic stream and slow modes (low M_{c_2}, high M_{c_1}) in shear layers between two supersonic streams. The reasons for the asymmetry remain unresolved, although preliminary models incorporating shock dissipation have been proposed.[7,10] Linear stability analysis also predicts fast and slow modes (for example, see Refs. 11 and 12). Even so, the prediction of Eq. (2), hereafter called the symmetric convective Mach number:

$$M_{c_\mathrm{sym}} = (U_1 - U_2)/(a_1 + a_2) \qquad (4)$$

is still a useful measure of the overall compressibility of a shear flow and will be used as such in this paper.

The very near field of a round jet is an annular shear layer, which, for a thickness much smaller than the radius of the potential core it surrounds, is similar to a planar shear layer. With increasing axial distance, however, that similarity fades as the shear layer consumes the pure jet fluid and eventually merges with itself, marking the end of the potential core. The end of the potential core is a region of intense turbulent activity, with formation of large eddies that govern entrainment and sound generation.[13] Hence, this is a region of special interest from the standpoints of mixing and noise.

In high-speed jets Mach-wave emission is a powerful source of noise and appears strongest from eddies near the end of the potential core, as revealed by many visualizations of such flows (Ref. 14, for example). Because of its impact on supersonic aircraft noise, Mach-wave radiation has been the subject of numerous experimental[13,15,16] and theoretical[17–19] investigations. Recent studies have shown that Mach-wave radiation can be avoided, or reduced, by surrounding the primary jet with a secondary flow such that the primary eddies become subsonic with respect to the secondary flow, while ensuring that the secondary eddies are subsonic with respect to the ambient. This method, called Mach-wave elimination,[20] has shown significant noise reduction in subscale tests.[21]

The preceding discussion underscores the importance of eddy convection, particularly in the region around the end of the potential core. Even though the compressible planar shear layer has been the subject of several evolution studies,[7–9,22] the authors are aware of only two evolution studies of high-speed jets,[23,24] both in the region of the near field where the flow would be better characterized as an axisymmetric shear layer. The effect of a secondary flow on the

*Graduate Student, Department of Mechanical and Aerospace Engineering. Member AIAA.
†Professor, Department of Mechanical and Aerospace Engineering. Member AIAA.

evolution of turbulence in high-speed jets has not been investigated, even though such coaxial jets are very common in propulsion and combustion applications. Furthermore, few of the preceding works used genuinely two-dimensional cross correlations to follow the eddies as spatial patterns of the quantity being visualized. Convection measurements near the end of the potential core are critical for the prediction and prevention of Mach waves. More generally, there is need for experimental databases to validate computations of large-scale structures and instability waves.[25]

To address these issues, an experimental program was designed to observe the evolution of eddies and measure their convective velocity in high-speed jets with and without secondary flow, concentrating in the vicinity of the end of the potential core. Some of the jets consisted of helium-air mixtures, which simulate hot-flow conditions. The investigation was carried out by visualizing the large structures and their evolution and subsequently extracting the convective velocity with two-dimensional cross correlations.

II. Experimental Methods

Flow Facility

Experiments were conducted in a coaxial jet facility (Fig. 1), a detailed description of which can be found in Ref. 20. Pure air or a mixture of helium and air were supplied to a coaxial nozzle arrangement and exhausted into ambient air. The inner nozzle, of 12.7-mm exit diameter, was designed by the method of characteristics for helium at Mach 1.5. When this nozzle is used for pure air or for helium-air mixtures, there is at most a discrepancy of 1.5% between the design and actual exit Mach numbers. Two outer convergent nozzles with exit diameters of 25.4 and 21.6 mm were employed. Helium-air mixtures were used to simulate approximately the density, speed of sound, and velocity of a heated jet. The total pressure of the primary flow was set at 370 kPa for pure air and 380 kPa for the helium-air mixture, resulting in pressure-matched jets. The helium-air mixture had a gas constant $R = 900$ J/kg K and a specific heat ratio $\gamma = 1.58$. Pressure transducers recorded the total pressures of the inner (primary) and outer (secondary) streams as well as the centerline pitot pressure. The total pressure measurements, together with the total temperature and gas constants, were used to calculate the flow conditions of the primary and secondary streams. Centerline pitot pressure data provided centerline Mach number distributions as a function of axial distance from the jet exit.

Table 1 summarizes the flow conditions. Subscripts p, s, and ∞ refer to the primary, secondary, and ambient conditions, respectively. Cases A1 and A2 comprise pure-air jets without and with a low-speed secondary flow, respectively. Case B is a helium-air jet with a low-speed secondary flow composed of air. Case C is the same helium-air jet with a higher-speed secondary flow consisting of air with a small dilution of helium. The Reynolds number of the primary jet, based on the jet diameter, was 6.8×10^5 for cases A1 and A2 and 4.3×10^5 for cases B and C.

Diagnostics

The diagnostic technique used to visualize the turbulent structure and its evolution is summarized in Fig. 2, in addition to the mixing layer geometry and nomenclature. The technique is based on laser-
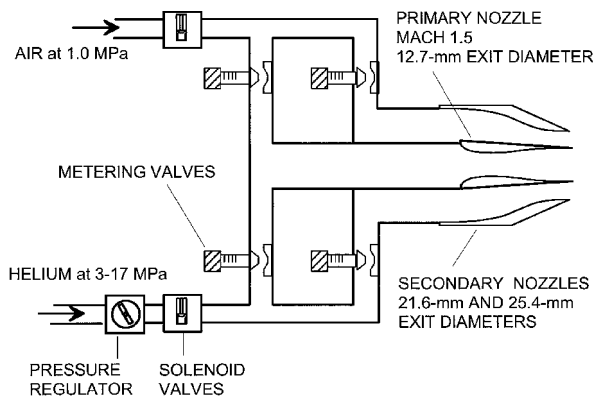
Table 1 Flow conditions

Parameter	A1	A2	B	C
			Case	
Gas_p	Air	Air	He + Air	He + Air
M_p	1.5	1.5	1.5	1.5
U_p, m/s	430	430	760	760
D_p, mm	12.7	12.7	12.7	12.7
ρ_p/ρ_∞	1.45	1.45	0.53	0.53
Gas_s	——	Air	Air	He + Air
M_s	——	0.37	0.37	0.82
U_s, m/s	——	130	130	320
D_s, mm	——	25.4	25.4	21.6
ρ_s/ρ_∞	——	1.04	1.04	0.83
$M_{c_{\text{sym}}}$	0.68	0.48	0.74	0.49

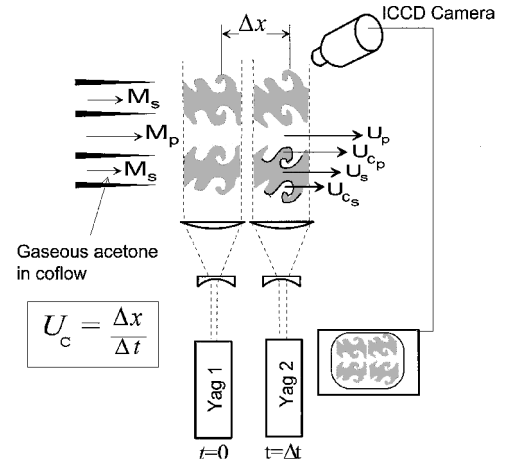**Fig. 2 Double-exposure PLIF system applied to the coaxial jet, shown with acetone seeded into the secondary flow.**

induced fluorescence of acetone[26] and in the past was employed in a study of turbulence evolution in planar shear layers.[9] Gaseous acetone was seeded alternatively into the primary and secondary streams. Injection was accomplished by supplying liquid acetone at very high pressures through atomizing nozzles placed in a duct approximately 1.5 m upstream of the jet plenum. The difficulty with employing acetone in supersonic flows is condensation caused by low temperature. We experimented with various levels of seeding, but condensation was difficult to avoid when acetone was injected into the primary, supersonic stream. For the pure-air jet we were able to acquire images with acetone in the primary stream showing minimal condensation. For the helium-air jet, which required higher levels of seeding because of its faster spreading rate, condensation of acetone in the primary stream was much more pronounced and prevented high-quality imaging of the flow.

We found, however, that condensation could largely be avoided when acetone was injected in a subsonic coflow surrounding the primary supersonic stream. The highest-quality pictures were obtained with a Mach 0.37 coflow of 25.4-mm exit diameter. For the pure-air jet case A1 represents acetone injection into the primary flow (without any secondary flow), whereas case A2 represents injection into a low-speed secondary flow surrounding the primary stream. For the helium-air jets acetone was injected only in the secondary flow (cases B and C).

The acetone was excited by the ultraviolet ($\lambda = 266$ nm) output of two independently pulsed Nd:YAG lasers. Their light was formed into two adjacent sheets, one from each laser, which sliced the jet at its centerline plane. Pulse energies were 20 mJ. Acetone fluoresced in the visible range ($\lambda \approx 480$ nm), thus marking the seeded fluid. The upstream laser was triggered first, and the downstream laser second with a time delay Δt. Both laser sheets were imaged by a single intensified charge-coupled device (CCD) camera (Princeton Instruments ICCD 576/RB). A short time delay Δt was initially chosen and gradually increased until turbulent features seen in the first sheet were captured in the second sheet. Images were analyzed by the cross-correlation method described next to yield the distance

Fig. 1 Coaxial supersonic jet facility.

Δx traveled by the identifiable features. The convective velocity was then computed by $U_c = \Delta x / \Delta t$. Precise synchronization of the lasers and camera with the solenoid valves was achieved using a data acquisition and control system on a 486DX-66 computer. Additional diagnostics included a nanosecond schlieren system, a microphone with 150-kHz frequency response (Bruel and Kjaer Model 4138), and a pitot probe, which traversed the centerline of the jet.

Cross-Correlation Method

The present study aims to characterize the evolution of large-scale turbulent structures in the mixing layer by obtaining convective velocity information from two-dimensional space-time correlations of the planar laser-induced fluorescence (PLIF) images. We focus on the most dominant instability of the flow, which we assume takes the form of large vortical structures. A slowly diffusing passive scalar, in this case acetone, is used to visualize the flow. We define eddies as phase-correlated two-dimensional patterns of this passive scalar, with the size of the pattern being of the same order as the local thickness of the shear layer. Thus for each image obtained, a template box was chosen large enough in the first laser sheet to contain a sizeable portion of the visually identified structure. The two-dimensional correlation scheme amounts to a phase alignment between the structure at $t = 0$ and its evolution at $t = \Delta t$. That is, the convective velocity of an eddy is determined by setting a criterion based on the shape of the structure in the template, which we try to match at a later time. This method, outlined next and further detailed in Papamoschou and Bunyajitradulya,[9] allows one to obtain evolution characteristics of large eddies by capturing the two-dimensional signature of these instability patterns.

The convective velocity was extracted from the double-exposure PLIF images according to the cross-correlation method depicted in Fig. 3. The image field is denoted by $F(\xi, \eta)$, where the value of the function F at a point (ξ, η) corresponds to the intensity at that pixel location. The left half of the image field corresponds to $t = 0$ and its right half to $t = \Delta t$. The size of the image field was 576×384 pixels. In the left half of F, we manually select a template $T(x, y)$, of size $M \times N$, containing the feature of interest. On average, templates were of size $M = 130$ and $N = 160$. The template slides over the entire image field in both the ξ and η directions. A spatial pattern of acetone is distinguished from the background by the fluctuations $T' = T - \langle T \rangle$ and $F' = F - \langle F \rangle$, where $\langle T \rangle$ and $\langle F \rangle$ denote the spatial average over the $M \times N$ region of the template and of the overlapping image, respectively. The template and overlapping image are correlated according to

$$C_{\mathrm{TF}}(\xi, \eta) = \frac{1}{MN} \sum_{x=1}^{M} \sum_{y=1}^{N} T'(x, y) F'(x + \xi, y + \eta) \quad (5)$$

When T' slides over the right half of F ($t = \Delta t$), Eq. (5) becomes a space-time correlation in two spatial dimensions. The correlation coefficient is defined as

$$R_{\mathrm{TF}}(\xi, \eta) = \frac{C_{\mathrm{TF}}(\xi, \eta)}{\sqrt{C_{\mathrm{FF}}(\xi, \eta) C_{\mathrm{TT}}}} \quad (6)$$

and takes the value of 1.0 for perfect correlation, i.e., when the template overlaps with itself.
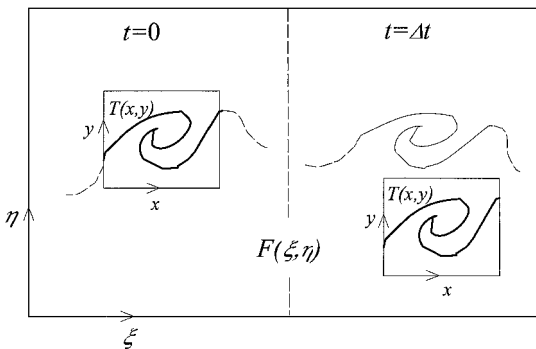

**Fig. 3   Two-dimensional cross-correlation method.**

III.   Results and Discussion

Schlieren Pictures and Noise Data

Figure 4a depicts a schlieren image of the pure-air jet of case A1. Images of case A2 are similar to those of case A1. The jet grows slowly and does not exhibit any visible Mach-wave radiation, i.e., its turbulent eddies are subsonic or sonic with respect to the ambient air. The helium-air jet of case B, shown in Fig. 4b, appears to grow much faster and emits Mach waves. The Mach waves of case B are inclined at an angle of 40 deg with respect to the jet axis, from which we infer that the eddies travel with Mach number 1.55 and convective velocity of 540 m/s with respect to the ambient. With the addition of a secondary flow to this jet, case C, Mach waves are substantially reduced,[20] as shown in Fig. 4c. The resulting noise attenuation is evident in the sound pressure level spectra of Fig. 5, obtained at a distance $r/D_p = 6$ from the jet exit and at an inclination
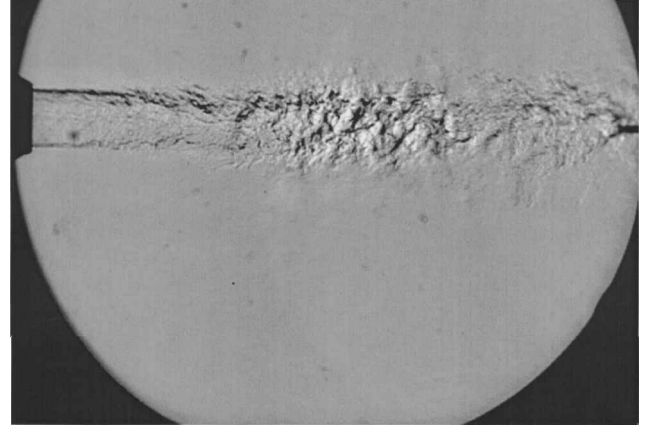
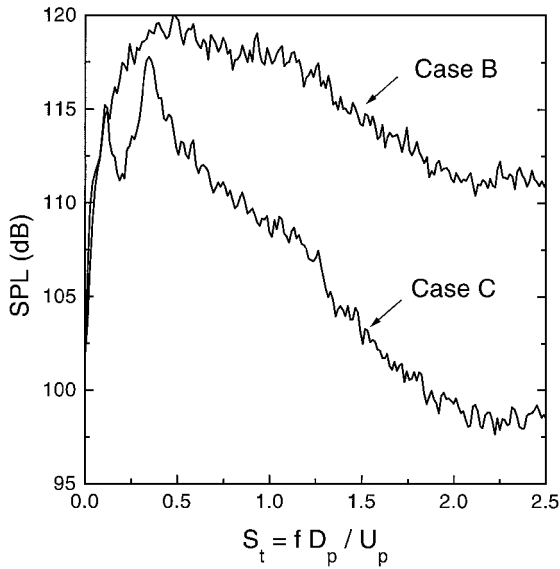**a) Case A1**
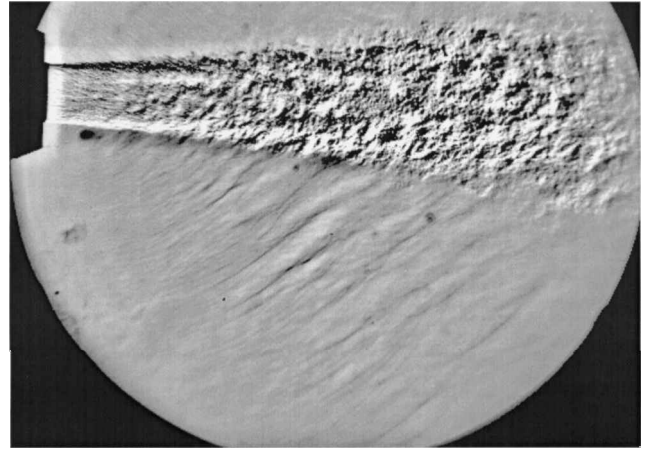
b) Case B
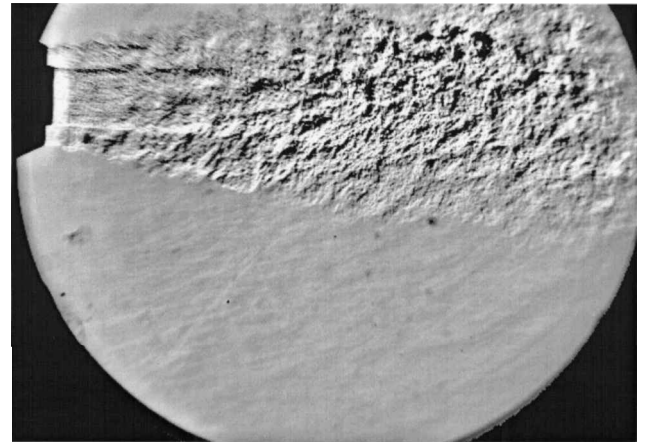
c) Case C

Fig. 4   Schlieren images.

Fig. 5 Sound-pressure-level spectra for cases B and C, compared at constant thrust via geometric scaling.[21]

Fig. 6 Centerline Mach-number distributions for a) the air jets and b) the helium-air jets.

of 45 deg with respect to the jet axis. The high-frequency component of the spectrum decreased by 12 dB. The reduction in the overall sound pressure level was 5 dB.

Centerline Mach-Number Distributions

Pitot measurements along the jet axis yielded the centerline Mach-number distributions, shown in Fig. 6. For the air jets case A2 had a longer potential core than did case A1 because of addition of the Mach 0.37 coflow, which reduced the growth rate of the primary mixing layer. For the helium-air jets increase of the coflow Mach number from 0.37 (case B) to 0.82 (case C) had minimal effect on the length of the potential core and caused only a slight reduction in the decay rate of the centerline Mach number. The length of the potential core for the simple air jet and for the helium-air jets is roughly the same, about 4–6 jet diameters, even though the helium-air jet has a larger spreading rate evident in Fig. 4b. The length of the potential core, however, depends not only on the spreading rate

Table 2   Convective velocities and Mach numbers

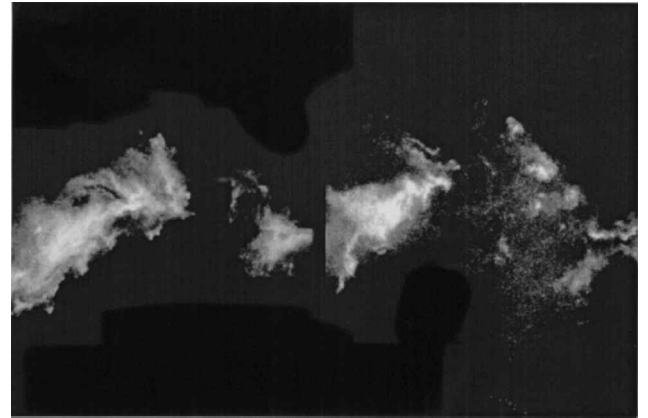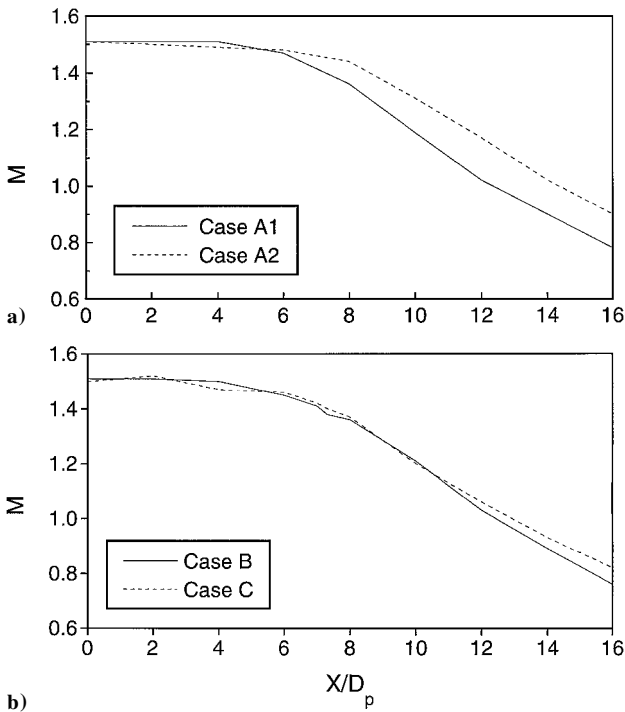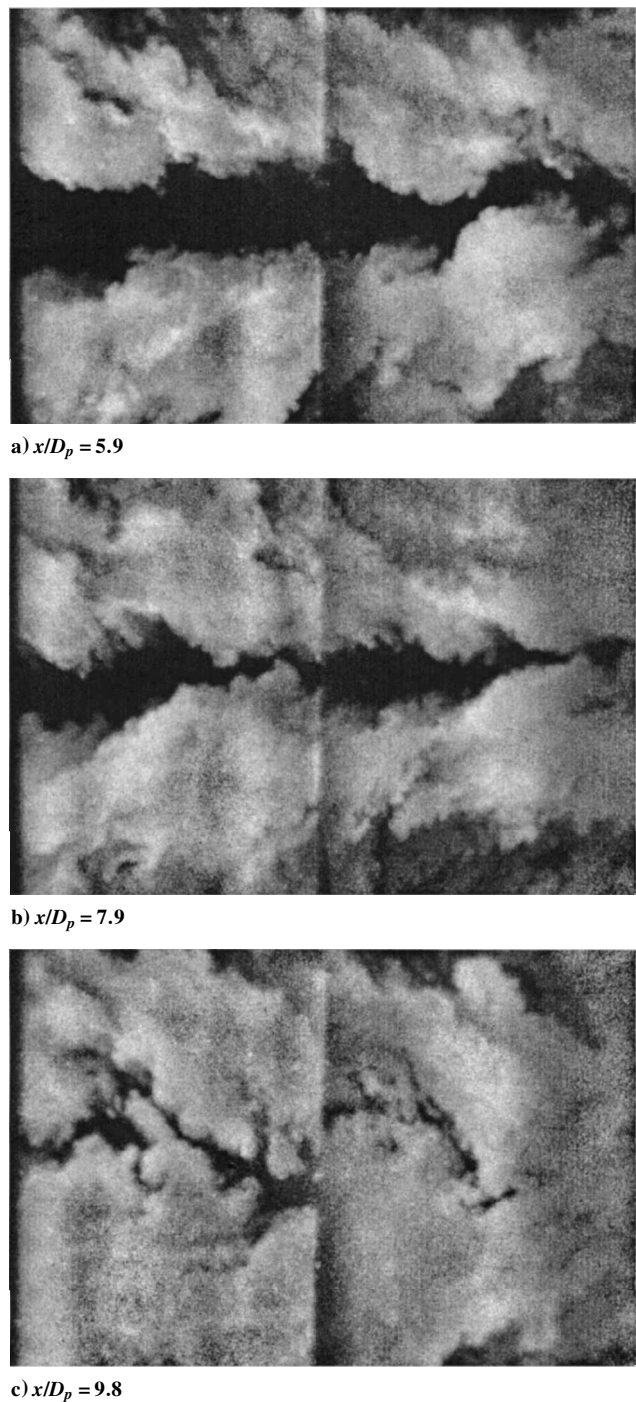| Case	x/D_p	$U_{c_{sym}}$, m/s	$U_{c_{avg}}$, m/s	σ, m/s	$M_{c_{sym}}$	M_{c1}	M_{c2}	d_{M_c}
A1	8.5	212	356	32	0.61	0.13	1.03	0.64
A1	10.0	194	298	33	0.56	0.22	0.86	0.45
A2	5.9	291	337	21	0.47	0.32	0.61	0.21
A2	7.9	286	321	24	0.46	0.34	0.56	0.16
A2	9.8	272	301	27	0.42	0.32	0.51	0.13
B	5.9	382	534	35	0.72	0.41	1.19	0.56
C	7.3	498	470	46	0.45	0.49	0.39	0.08
C (s/∞)	2.6	152	142	8	0.43	0.46	0.41	0.03

Fig. 7   PLIF image for the air jet of case A1 at $x/D_p = 10$.

but also on the geometry of the dividing streamline, which may be inclined outward in the helium-air jets.

For the air jets the centerline velocity was calculated from the centerline Mach number by assuming constant total temperature. The helium-air jets calculation of velocity also requires the concentration field, which was not measured. However, for the near field of the jet we assumed a constant gas constant R to obtain an approximate centerline velocity distribution.

PLIF Images and Cross Correlations

We discuss now the qualitative features of the turbulent structure revealed in the PLIF images and the convective velocity measurements obtained from the cross correlations. The x/D_p locations quoted next correspond to the distance from the jet exit to the middle of the imaging region. For ease of reference, the ensemble-averaged convective velocity values for each case and location are listed in Table 2, together with their standard deviation and their prediction from the symmetric model of Eq. (3).

A representative PLIF image of case A1 is shown in Fig. 7. Acetone was injected in the primary flow and provided good views of the turbulent structure, although some condensation is evident. The location $x/D_p = 10.0$, which is near the end of the potential core, offered the best images with this injection scheme. Upstream of this location, the structures were too small to follow, and condensation was more pronounced. Downstream, the flow mixed faster, and the acetone signal dropped substantially from the first sheet to the second.

Acetone injection in a subsonic flow surrounding the primary stream resulted in better and more consistent visualizations, without any condensation. Images for case A2 are presented in Figs. 8a–8c for locations $x/D_p = 5.9$, 7.9, and 9.8, respectively. The primary flow is seen as the dark central region surrounded by the bright secondary flow. For each image one can follow large-scale features from the first sheet to the delayed sheet, although they do not appear as organized roller-type structures often seen in subsonic experiments. As we move downstream, the secondary stream is further entrained and mixed into the primary flow, with the structures retaining the same general shape visualized in the first sheet.

For the air jets of cases A1 and A2, 100 double-pulse PLIF images were used to extract the convective velocity of the primary eddies. Seventy-seven of these images were cross correlated using

a) $x/D_p = 5.9$

b) $x/D_p = 7.9$

c) $x/D_p = 9.8$

Fig. 8   PLIF image for the air jet of case A2.

Fig. 9   PLIF image and cross correlation for the air jet of case A2, where $x/D_p = 7.9$ and $\Delta t = 80\,\theta$ s.

Fig. 10   Ensemble-averaged convective velocities vs axial distance for the air jets. The mean centerline velocity distributions are also shown.

the scheme described earlier. An example is shown in Fig. 9 for case A2 at $x/D_p = 7.9$. The template chosen for the image is highlighted by a white box. When the template containing the turbulent eddy matches itself, the correlation coefficient is 1.0, seen as the first peak in the left half of the corresponding contour plot. The second peak in the right half indicates the best match of the template with the evolution of the eddy. Typically, the second peak of the correlation was higher than 0.6. Values below this threshold led to rejection of the measurement.

Manual measurements of U_c for the air jet were made for the remaining 23 images. Even though features in those images were easily followed with the eye, cross correlations give poor results for some images because of the rapid growth of the eddies from the left exposure to the right. The manual measurements are in good agreement with the cross-correlation measurements. For the air jets an average of 20 images were analyzed for each downstream position by cross correlation and manual methods. Figure 10 plots the
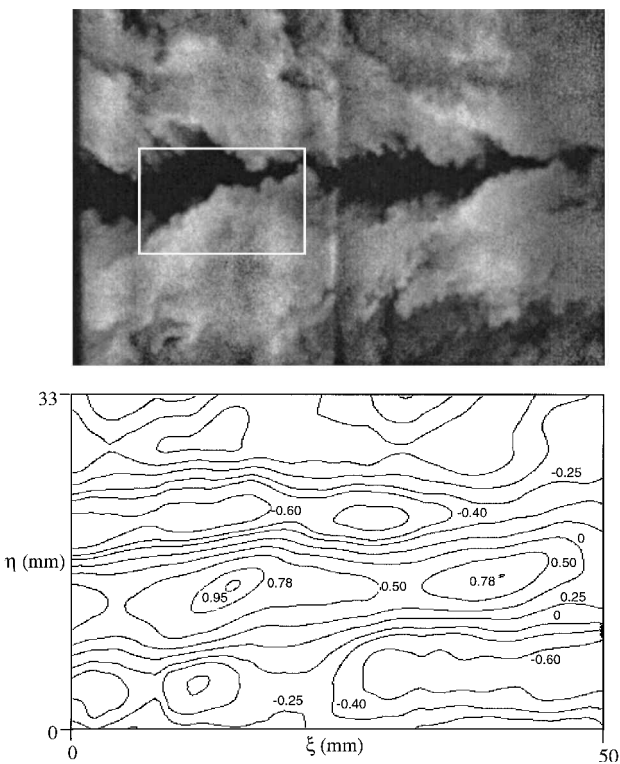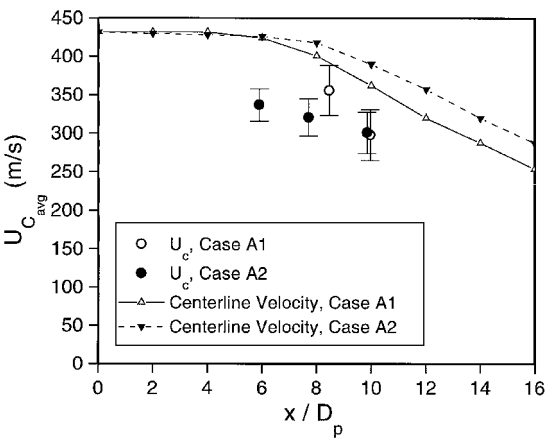
corresponding ensemble-averaged values. The standard deviations are all within 11% of the mean, indicating a narrow distribution of convective velocities. Included in Fig. 10 is the mean centerline velocity, inferred from pitot measurements. The convective velocity follows the centerline velocity at a ratio of about 80%. The upstream measurement for case A1 deviates slightly from this trend, which could be a result of bias caused by the condensation of acetone. From Table 2 the measured convective velocity is on the average 61% higher than the symmetric prediction for case A1 and 13% higher for case A2. These deviations indicate the existence of fast modes in both air-jet cases.

In the helium-air jets of cases B and C, acetone was injected only in the coflow. Images acquired for these cases indicate that the mixing layers grow faster than those of the air jets, consistent with the schlieren visualizations. In addition, the large-scale structures appear to be more disorganized. Figures 11 and 12 present PLIF image pairs and cross correlations for cases B and C, respectively. As in the air jets, only correlations generally above 0.6 were retained in the calculation of the convective velocity. An example of a poor correlation is shown in Fig. 13. The reason for the bad correlation
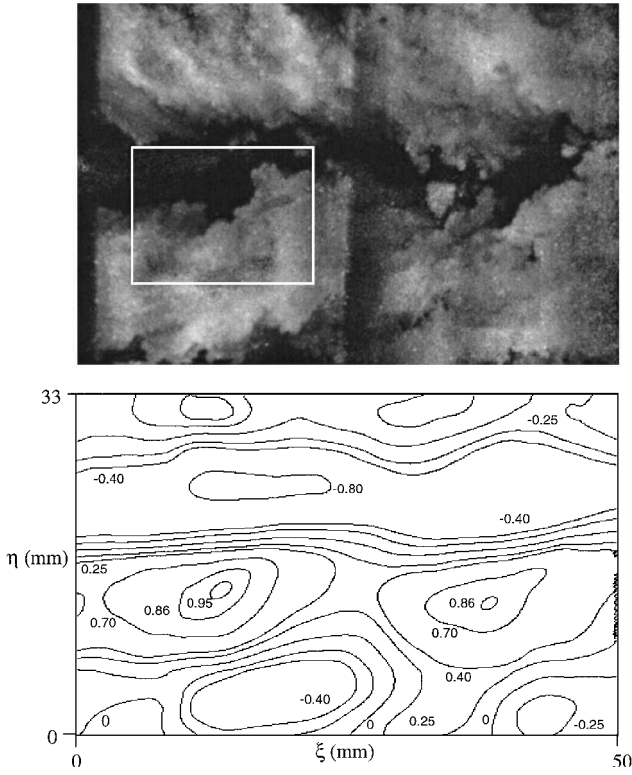
Fig. 11   PLIF image and cross correlation for the helium-air jet of case B, where $x/D_p = 5.9$ and $\Delta t = 45\,\theta$ s.
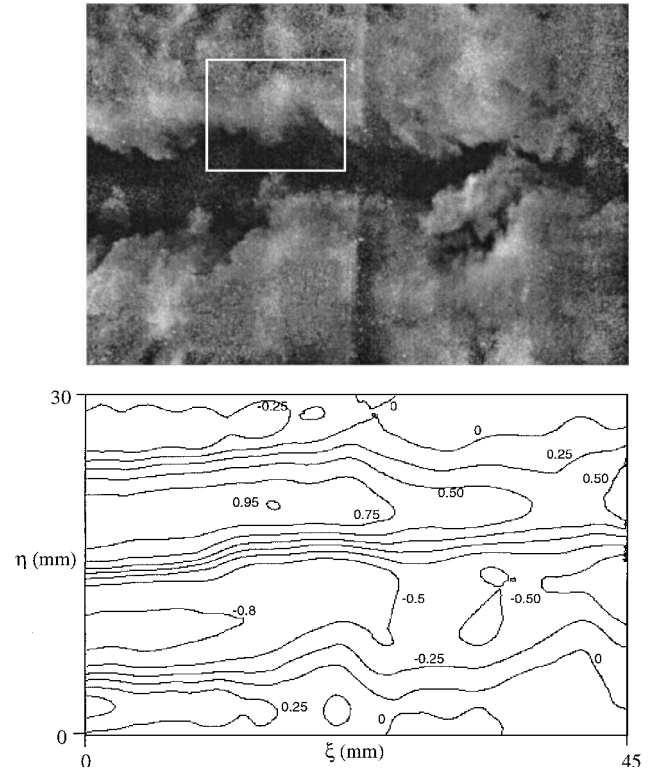

Fig. 13   PLIF image and cross correlation for the helium-air jet of case C at $x/D_p = 5.7$. The new mass of fluid in the delayed sheet results in a poor correlation and rejection of this measurement.
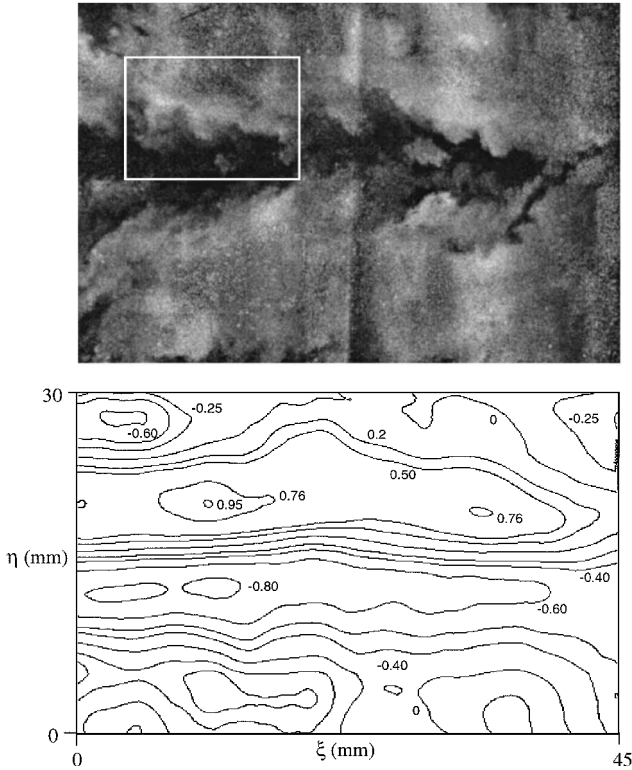

Fig. 12   PLIF image and cross correlation for the helium-air jet of case C, where $x/D_p = 7.3$ and $\Delta t = 48\,\theta$ s.

is the appearance of a new lump of fluid in the second sheet not captured in the first sheet. This occurred often in the helium-air jets and is the result of the prevalence of azimuthal motions with increasing compressibility. As a result, the data rejection rate for the helium-air jets was much higher than that for the air jets.

With addition of a Mach 0.82 coflow to the helium-air jet, case C, we had the opportunity to observe eddies between the primary and secondary flows and between the secondary flow and the ambient.

Of course, the time delays had to be different for tracking primary and secondary eddies. Moreover, the coflow reduced the growth rate of the primary mixing layer, forcing us to shift the imaging location slightly downstream to $x/D_p = 7.3$ to capture and follow large primary eddies. As far as the turbulent structure between primary and secondary flows is concerned, there are no discernible differences from case B. The mixing layer between the secondary flow and the ambient for case C is shown in Fig. 14, where the field of view was shifted to capture all of its features. The growth rate of this subsonic mixing layer is larger than that of the primary mixing layer. The secondary mixing layer exhibited roller-type structures reminiscent of those observed in incompressible shear layers.[1]

For the helium-air jets 47 pictures were analyzed, 35 with the cross-correlation routine and the rest manually. Figure 15 presents a plot of the ensemble-averaged convective velocity vs axial location for the primary eddies of case B and for the primary and secondary eddies of case C. For case B the ensemble-averaged primary convective velocity is 534 m/s (70% of the jet exit velocity), which is in good agreement with the value of 540 m/s inferred from the inclination of the Mach waves in the schlieren photograph of Fig. 4b. The measured value of U_c is 40% higher than its symmetric value. Addition of a Mach 0.82 secondary flow to this jet, case C, decreases the primary convective velocity by 12%. As mentioned earlier, for case C we had to shift our imaging region relative to case B from $x/D_p = 5.9$ to 7.3. The corresponding drop in center-line Mach number, obtained from Fig. 6b, is 3%. It is reasonable to expect a centerline velocity drop of the same magnitude, around 3%. Thus, the reduction of U_c with increasing coflow Mach number is not an artifact of our shift in measuring location. Rather, it indicates an interesting, counterintuitive trend, which we believe is caused by the reduced compressibility of case C and which we will attempt to explain later. In case C, the turbulent eddies between the secondary flow and the ambient air convect at a speed of 142 m/s, which is very close to the prediction of 152 m/s from the symmetric formula, Eq. (3).

A summary of the results is presented in Table 2. The convective Mach numbers are based on the ensemble-averaged value of U_c at each location and on the local centerline velocity. The measured convective Mach numbers M_{c_1} and M_{c_2} are plotted vs each other in
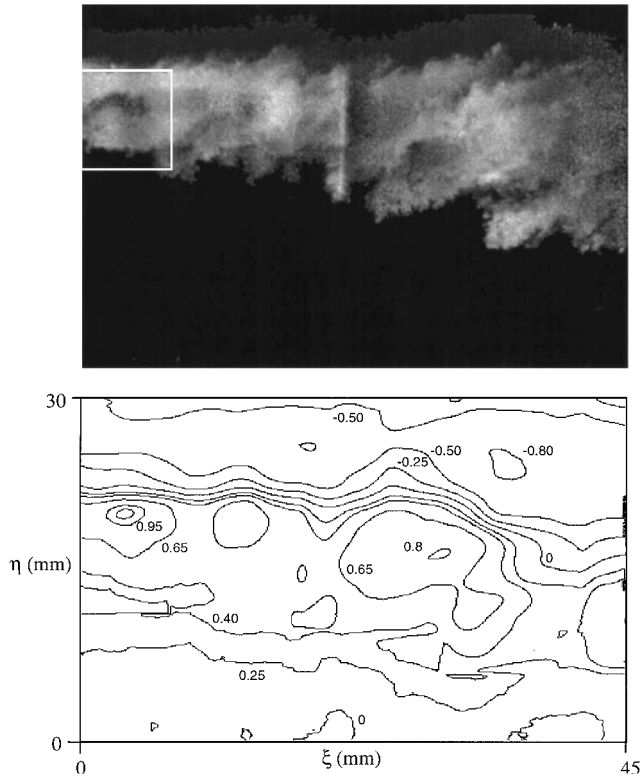
Fig. 14   PLIF image and cross correlation of the secondary shear layer of case C, where $x/D_p = 2.6$ and $\Delta t = 190\,\theta$ s.
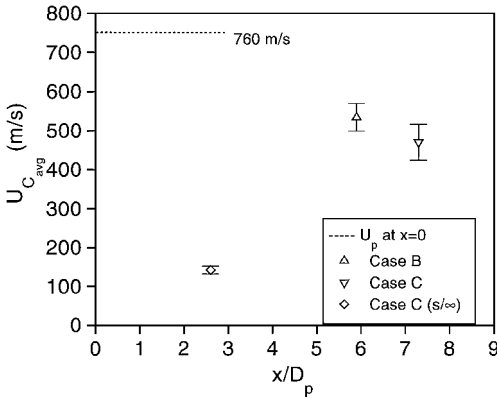

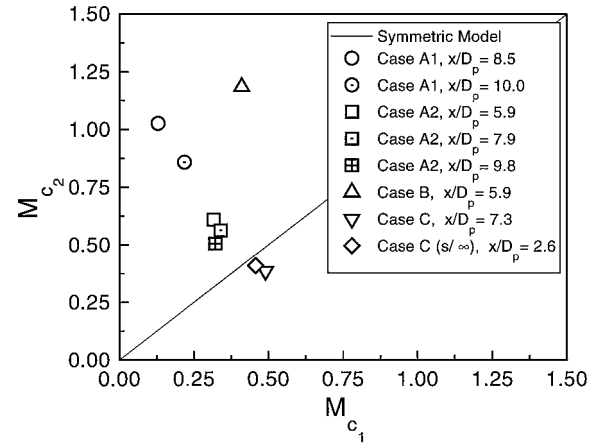Fig. 15   Ensemble-averaged convective velocity measurements for the helium-air jets of cases B and C.

Fig. 16   Convective Mach numbers plotted vs each other.
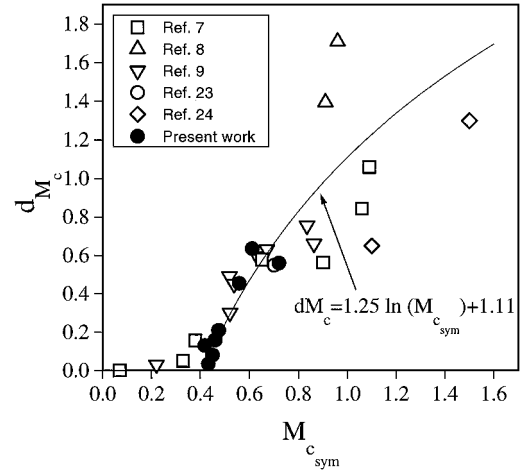
Fig. 17   Convective Mach-number deviation from the symmetric model.

Fig. 16. The diagonal line on this diagram represents the symmetric model, Eq. (2). As already noted, the eddies in the air jets travel faster than predicted by the symmetric model, creating a large M_{c_2} and a small M_{c_1}. This asymmetric behavior is more pronounced in the helium-air jet of case B because of its higher compressibility. The supersonic value of M_{c_2} in case B indicates that the primary eddies travel supersonically relative to the secondary flow, consistent with generation of Mach waves. The Mach 0.82 secondary flow of case C lowers the relative speed of the primary eddies, thus reducing M_{c_2} of the primary mixing layer from 1.19 to 0.39. The reduction of the primary convective velocity with increasing coflow Mach number, seen in Fig. 15, contributes further to this reduction of M_{c_2}. In case C the values of M_{c_2} are subsonic for both the primary and secondary mixing layers, leading to substantial weakening of the Mach waves as seen in Fig. 4c. Furthermore, the convective Mach numbers of the secondary eddies of case C fall almost exactly on the symmetric line of the $M_{c_1} - M_{c_2}$ diagram.

The deviation from the symmetric model can be expressed in terms of the distance

$$d_{M_c} = \sqrt{\left(M_{c_1} - M_{c_{sym}}\right)^2 + \left(M_{c_2} - M_{c_{sym}}\right)^2} \qquad (7)$$

of a measurement from its symmetric value on the $M_{c_1} - M_{c_2}$ diagram.[9] Figure 17 plots this distance vs $M_{c_{sym}}$ for the present measurements as well as the measurements of previous experimental investigations, which measured U_c in planar and axisymmetric shear layers. The results of our study coincide very well with the shear-layer data, even though our measurements were done in a messy region of the flow with nonconstant freestream velocity. The overall trend shows a rapid departure from symmetry as $M_{c_{sym}}$ exceeds roughly 0.41. Despite the scatter of the data in the literature at high $M_{c_{sym}}$, the departure from symmetry is unmistakable and reminiscent of that found by Jackson and Grosch in their plots of phase speed vs Mach number for a linear disturbance.[11]

Reduction of $M_{c_{sym}}$ should lead to a smaller departure from symmetry, which in turn should drive U_c closer to its symmetric value. By increasing the secondary velocity of the helium-air jet (case B to case C), we reduced $M_{c_{sym}}$ from 0.72 to 0.45. This resulted in a U_c very close to its symmetric value, as seen in Table 2. We believe that this explains the reduction in U_c from case B to case C.

Model for the Convective Mach Numbers

The good correlation of d_{M_c} vs $M_{c_{sym}}$ shown in Fig. 17, especially in the region of moderate $M_{c_{sym}}$, leads to an approximate model for the convective Mach number that can be applied to flows of practical interest. The departure from symmetry is approximated by the logarithmic function

$$d_{M_c} = \begin{cases} 1.25 \, \ell n \, M_{c_{sym}} + 1.11, & M_{c_{sym}} > 0.41 \\ 0, & M_{c_{sym}} \leq 0.41 \end{cases} \qquad (8)$$

which fits the data better than does the linear model suggested earlier by Papamoschou and Bunyajitradulya.[9] Inverting Eq. (7) and using

the definitions of Eq. (1), we relate the convective Mach numbers to the departure from symmetry as follows:

$$M_{c2} = M_{c_{\text{sym}}} \pm \frac{d_{M_c}}{\sqrt{1 + (a_2/a_1)^2}}$$

$$M_{c1} = M_{c_{\text{sym}}} \pm \frac{-d_{M_c}}{\sqrt{1 + (a_1/a_2)^2}} \qquad (9)$$

with $M_{c_{\text{sym}}}$ given by Eq. (4). Empirical evidence indicates that the plus sign (fast modes) should be used for shear layers between a supersonic stream and a subsonic stream and the minus sign (slow modes) for shear layers between two supersonic streams. Once M_{c1} or M_{c2} is determined, the convective velocity is calculated from Eq. (1). The accuracy of the model is no better than the accuracy of the underlying measurements. In our experience with a large variety of supersonic jets, the model predictions have agreed very well with the convective speed inferred from the slopes of Mach waves or from the directivity of the acoustic field.

IV. Conclusions

The morphology and evolution of turbulent eddies in coaxial Mach 1.5 jets with primary velocities of 430 and 760 m/s were studied experimentally. A double-exposure, PLIF system enabled visualization of the flow and of its evolution. Two-dimensional cross correlations yielded the convective velocities of the eddies in the primary and secondary mixing layers. Schlieren photography, noise measurements, and centerline pitot surveys complemented the study. The general observation is that, for symmetric convective Mach numbers above 0.4, the eddy convection is faster than that predicted by prevailing models. In the 430-m/s jet, which was composed of air, eddies in the primary shear layer traveled with 80% of the local centerline mean velocity. In the 760-m/s jet, which consisted of a helium-air mixture, the convective velocity was 70% of the jet exit velocity and resulted in Mach-wave emission. Addition of a Mach 0.82 secondary flow to the helium-air jet reduced this convective velocity by 12%. The secondary flow rendered all relative turbulent motions subsonic, leading to near elimination of the Mach waves and substantial noise reduction. The convective Mach-number measurements are in general agreement with those obtained in planar or axisymmetric shear layers, even in the region past the potential core of the jet. An approximate model for predicting convective Mach numbers is presented.

Acknowledgments

References

[1]Brown, G. L., and Roshko, A., "On Density Effects and Large Structure in Turbulent Mixing Layers," *Journal of Fluid Mechanics*, Vol. 64, Pt. 4, July 1974, pp. 775–816.

[2]Ho, C.-M., and Huerre, P., "Perturbed Free Shear Layers," *Annual Review of Fluid Mechanics*, Vol. 16, 1984, pp. 365–424.

[3]Morris, P. J., Giridharan, M. G., and Lilley, G. M., "On the Turbulent Mixing of Compressible Free Shear Layers," *Proceedings of the Royal Society of London, Series A: Mathematical and Physical Sciences*, Vol. 431, No. 1882, 1990, pp. 219–243.

[4]Dimotakis, P. E., "Two-Dimensional Shear Layer Entrainment," *AIAA Journal*, Vol. 24, No. 11, 1986, pp. 1791–1796.

[5]Clemens, N. T., and Mungal, M. G., "Two- and Three-Dimensional Effects in the Supersonic Mixing Layer," *AIAA Journal*, Vol. 30, No. 4, 1992, pp. 973–981.

[6]Papamoschou, D., and Roshko, A., "The Compressible Turbulent Shear Layer: An Experimental Study," *Journal of Fluid Mechanics*, Vol. 197, Dec. 1988, pp. 453–477.

[7]Papamoschou, D., "Structure of the Compressible Turbulent Shear Layer," AIAA Paper 89-0216, Jan. 1989.

[8]Hall, J. L., Dimotakis, P. E., and Rosemann, H., "Experiments in Nonreacting Compressible Shear Layers," *AIAA Journal*, Vol. 31, No. 12, 1993, pp. 2247–2254.

[9]Papamoschou, D., and Bunyajitradulya, A., "Evolution of Large Eddies in Compressible Shear Layers," *Physics of Fluids*, Vol. 9, No. 3, 1997, pp. 756–765.

[10]Dimotakis, P. E., "Turbulent Free-Shear Layer Mixing and Combustion," *Progress in Astronautics and Aeronautics*, Vol. 137, 1991, pp. 265–340.

[11]Jackson, T. L., and Grosch, C. E., "Inviscid Spatial Stability of a Compressible Mixing Layer," *Journal of Fluid Mechanics*, Vol. 208, Nov. 1989, pp. 609–637.

[12]Day, M. J., Reynolds, W. C., and Mansour, N. N., "The Structure of the Compressible Reacting Mixing Layer: Insights from Linear Stability Analysis," *Physics of Fluids*, Vol. 10, No. 4, 1998, pp. 993–1007.

[13]Bishop, K. A., Ffowcs Williams, J. E., and Smith, W., "On the Noise Sources of the Unsuppressed High-Speed Jet," *Journal of Fluid Mechanics*, Vol. 50, Pt. 1, Nov. 1971, pp. 21–32.

[14]Nagai, M., "Mechanism of Pseudo-Shock Wave in Supersonic Jet," *Bulletin of Japan Society of Mechanical Engineers*, Vol. 26, No. 212, 1983, pp. 207–211.

[15]McLaughlin, D. K., Morrison, G. L., and Troutt, T. R., "Experiments on the Instability Waves in a Supersonic Jet and Their Acoustic Radiation," *Journal of Fluid Mechanics*, Vol. 69, Pt. 1, May 1975, pp. 73–95.

[16]Troutt, T. R., and McLaughlin, D. K., "Experiments on the Flow and Acoustic Properties of a Moderate Reynolds Number Supersonic Jet," *Journal of Fluid Mechanics*, Vol. 116, March 1982, pp. 123–156.

[17]Tam, C. K. W., Chen, P., and Seiner, J. M., "Relationship Between Instability Waves and Noise of High Speed Jets," *AIAA Journal*, Vol. 30, No. 7, 1992, pp. 1747–1752.

[18]Seiner, J. M., Bhat, T. R. S., and Ponton, M. K., "Mach Wave Emission from a High Temperature Supersonic Jet," *AIAA Journal*, Vol. 32, No. 12, 1994, pp. 2345–2350.

[19]Mitchell, B. E., Lele, S. K., and Moin, P., "Direct Computation of Mach Wave Radiation in an Axisymmetric Supersonic Jet," *AIAA Journal*, Vol. 35, No. 10, 1994, pp. 1574–1580.

[20]Papamoschou, D., "Mach Wave Elimination in Supersonic Jets," *AIAA Journal*, Vol. 35, No. 10, 1997, pp. 1604–1611.

[21]Papamoschou, D., and Debiasi, M., "Noise Measurements in Supersonic Jets Treated with the Mach Wave Elimination Method," AIAA Paper 98-0280, Jan. 1998.

[22]Elliott, G. S., Samimy, M., and Arnette, S. A., "The Characteristics and Evolution of Large-Scale Structures in Compressible Mixing Layers," *Physics of Fluids*, Vol. 7, No. 4, 1995, pp. 864–876.

[23]Fourguette, D. C., Dibble, R. W., and Mungal, M. G., "Time Evolution of the Shear Layer of a Supersonic Axisymmetric Jet," *AIAA Journal*, Vol. 29, No. 7, 1991, pp. 1123–1130.

[24]McIntyre, S. S., and Settles, G. S., "Optical Experiments on Axisymmetric Compressible Turbulent Mixing Layers," AIAA Paper 91-0623, Jan. 1991.

[25]Dahl, M. D., and Morris, P. J., "Noise from Supersonic Coaxial Jets, Part 2: Normal Velocity Profile," *Journal of Sound and Vibration*, Vol. 200, No. 5, 1997, pp. 665–699.

[26]Lozano, A., Yip, B., and Hanson, R. K., "Acetone: A Tracer for Concentration Measurements in Gaseous Flows by Planar Laser-Induced Fluorescence," *Experiments in Fluids*, Vol. 13, No. 6, 1992, pp. 369–376.

M. Samimy
Associate Editor